crystals

MDPI

Article

Ultrathin g-C_3N_4 Nanosheet-Modified BiOCl Hierarchical Flower-Like Plate Heterostructure with Enhanced Photostability and Photocatalytic Performance

Tiekun Jia [1,*], Jili Li [1], Fei Long [2], Fang Fu [1], Junwei Zhao [1], Zhao Deng [3,*], Xiaohui Wang [4] and Ying Zhang [1]

1 School of Materials Science and Engineering, Luoyang Institute of Science and Technology, Luoyang 471023, China; lijili328@126.com (J.L.); fufang1@126.com (F.F.); jwzhao2013@sinano.ac.cn (J.Z.); q1067947253@126.com (Y.Z.)
2 School of Materials Science and Engineering, Guilin University of Technology, Guilin 532100, China; longf@glut.edu.cn
3 State Key Lab of Materials Synthesis and Processing, Wuhan University of Technology, Wuhan 430070, China
4 Luoyang Orthopedic Hospital of Henan Province, Luoyang 471013, China; wxhui070724@163.com
* Correspondence: tiekunjia@126.com or tkjia@whut.edu.cn (T.J.); dengzhao@whut.edu.cn (Z.D.); Tel./Fax: +86-379-65928196 (T.J.)

Academic Editor: Julien Haines
Received: 22 July 2017; Accepted: 30 August 2017; Published: 31 August 2017

Abstract: A novel ultrathin g-C_3N_4 nanosheet-modified BiOCl hierarchical flower-like plate heterostructure (abbreviated as BC/CN) was constructed via a thermal polymerization of urea precursor followed with hydrolysis route. The as-prepared samples were well characterized by various analytical techniques. The morphological observation showed that hierarchical flower-like BiOCl nanoplates were discretely anchored on the surface of ultra-thin C_3N_4 nanosheets. The photocatalytic performance of the as-prepared photocatalysts was evaluated by degradation of methylene blue (MB) under visible-light irradiation. The results showed that BC/CN photocatalyst exhibited enhanced photostability and photocatalytic performance in the degradation process. On the basis of experimental results and the analysis of band energy structure, it could be inferred that the enhanced photocatalytic performance of BC/CN photocatalyst was intimately related with the hybridization of hierarchical flower-like BiOCl nanoplates with ultrathin g-C_3N_4 nanosheets, which provided good adsorptive capacity, extended light absorption, suppressed the recombination of photo-generated electron–hole pairs, and facilitated charge transfer efficiently.

Keywords: BiOCl/g-C_3N_4; heterostructure; visible light; photocatalytic performance

1. Introduction

Environmental pollution and energy crisis are becoming a highly serious threat to humanity's existence and development, while photocatalysis is promising to be one of the most economic and ecologically safe approaches for settling the above-mentioned problems. For this purpose, many studies have been devoted to developing modified traditional TiO_2 or TiO_2-alternative photocatalysts for improving their photocatalytic performance [1–5]. As an important representative of BiOX (X = Cl, Br, I) species (p-type semiconductors), BiOCl has unique layered structure built by interlacing (Bi_2O_2) slabs with double chlorine slabs, leading to the formation of self-built internal static electric fields. Besides above, it also has the merits of good chemical stability, excellent resistance to photocorrosion, non-toxicity and earth abundance [6–8]. Previous study reported that the two

dimensional (2D) BiOCl showed layered structure, which is conductive to the transfer and separation of the photo-generated electron–hole pairs [9]. Thereby, BiOCl exhibits good photocatalytic performance for degrading organic pollutants in wastewater, such as Rhodamine B, acetophenone, etc. [10–12]. However, bare BiOCl can only absorb a small portion of the total irradiated natural sunlight due to its wide bandgap (3.19–3.60 eV), which limits the efficient utilization of solar energy. Nowadays, wide bandgap and low quantum efficiency of BiOCl based photocatalysts are regarded as the main cause of low visible-light photocatalytic efficiency. Consequently, great efforts have been made to enhance the photocatalytic performance by modifying BiOCl with other semiconductors, e.g., Bi_2S_3/BiOCl [13], $Bi_2W_xMo_{1-x}O_6$/BiOCl [14], BiOI/BiOCl [15], $BiVO_4$/BiOCl [16], WO_3/BiOCl [17], $Bi_2O_2CO_3$/BiOCl [18], and BiOCl/Bi_2O_3 [19]. All of the above-mentioned reports are intriguing and impressive, however, it still remains a great challenge to design facile and effective approaches for synthesizing novel BiOCl based photocatalysts with wide spectral response range and high photocatalytic efficiency.

Graphitic carbon nitride (g-C_3N_4), a polymeric metal-free n-type semiconductor with an indirect narrow bandgap of 2.7 eV, has become a hotspot in photocatalysis due to its facile synthesis, high thermal and chemical stability, excellent optical characteristics and low cost, thus it has been extensively studied as a visible light driven photocatalyst for organic pollutant photodegradation and hydrogen production from water photo-splitting [20–32]. However, bare C_3N_4 has the intrinsic drawbacks of poor mass diffusion, low quantum efficiency and high recombination rate of photo-generated electron–hole pairs, leading to the fact that its photodegradation rate is far from optimal level [24–37]. According to previous reports [27–38], constructing heterostructures with two well matched energy level semiconductors is an effective strategy to extend absorption range and achieve a rapid and effective separation of electron–holes pairs. Feng et al. [39] reported the preparation of Bi@BiOCl/g-C_3N_4 with excellent photocatalytic efficiency, using a solvothermal method followed by a surface oxidation treatment. In this hybrid structure, Bi spheres were deposited on porous C_3N_4 and BiOCl was on the surface of Bi spheres except for the interface between g-C_3N_4 and metallic Bi. Shan et al. [40] prepared g-C_3N_4/bismuth-based oxide composites, using Bi_2O_3 or CH_5N_3·HCl and g-C_3N_4 as starting materials. The results showed that some thin flakes of $Bi_2O_2CO_3$ or BiOCl sprouted from the g-C_3N_4 bulk, and the degradation rate of MO over 75% g-C_3N_4/BiOCl photocatalyst reached 100% after 5 h visible light irradiation. Aghdam et al. [41] reported the synthesis of BiOI/BiOCl/g-C_3N_4 ternary photocatalyst and investigated the proposed photocatalytic mechanism for the degradation of acid orange 7. However, the above obtained g-C_3N_4 based photocatalysts presented a low BET surface area (6.7–32 m^2/g), which probably limited their absorption capability involved in the photodegradation reactions [42–45]. In addition, it has confirmed that large surface area and the p-n heterostructure are beneficial for achieving excellent photocatalytic activity of g-C_3N_4 based photocatalysts [42–49]. Based on the consideration mentioned above, provided that 2D BiOCl nanoplates combine with g-C_3N_4 ultrathin nanosheets to form plate-on-sheet heterostructure with large surface contact, this novel p-n BC/CN heterostructure photocatalyst is promising to exhibit significantly enhanced visible light photoactivity for degrading pollutants. Unfortunately, limited research work is focused on addressing this issue in BC/CN system up to now. Therefore, it is of great interest to explore facile approaches for the synthesis of novel p-n BC/CN heterostructure and investigate the proposed mechanism of the enhanced photoactivity.

In this work, hierarchical flower-like BiOCl nanoplates/ultrathin g-C_3N_4 nanosheet heterostructure was constructed via a thermal polymerization followed by hydrolysis method. First, ultrathin g-C_3N_4 nanosheets were prepared by one-step thermal polymerization of urea precursor. Subsequently, hierarchical flower-like BiOCl nanoplates were formed in situ on the n-g-C_3N_4 ultrathin nanosheets via a simple hydrolysis route. The phase, surface composition, morphologies and optical property of the as-prepared samples were well characterized, and the visible-light photocatalytic performance of photocatalysts was examined for the degradation of methylene blue (MB). The separation and migration of the photoexcited electron–hole pairs of the photocatalysts were investigated by photoluminescence (PL) spectroscopy measurement, while the active species involved

in the photodegradation process were investigated by free radicals and hole scavenging experiments. The proposed mechanism of the enhanced photocatalytic performance over BC/CN heterostructure was examined based on experimental results and the analysis of band energy structure.

2. Results and Discussion

2.1. Phase Structure and Morphology

XRD was utilized to identify the crystal phase structure of the as-prepared samples. Figure 1 shows the XRD patterns of the g-C_3N_4, $N_{0.45}B_{0.55}$ and BiOCl samples. As is seen in Figure 1, the pronounced diffraction peak at 27.7° of g-C_3N_4 is indexed to (002) planes, which is a characteristic inter-planar stacking reflection of conjugated aromatic systems. The weak diffraction peak at 13.1° is indexed to (100) diffraction planes of g-C_3N_4, corresponding to the interlayer structural packing. With respect to BiOCl, all the diffraction peaks are in good accordance with those of tetragonal-phase BiOCl reported in JCPDS card (06-0249). The diffraction peaks with 2θ values of 11.98°, 24.10°, 25.86°, 32.50°, 33.45°, 34.48°, 36.54°, 40.89°, 46.64°, 48.35°, 49.70°, 54.10°, 55.14°, 58.48°, 60.67°, 68.16°, 70.06°, and 77.58° can be indexed to (001), (002), (101), (110), (102), (111), (003), (112), (200), (201), (113), (211), (104), (212), (114), (220), (214) and (310) planes of BiOCl, respectively. In the case of $N_{0.45}B_{0.55}$, the diffraction peaks of BiOCl are obviously observable, and the typical pattern for g-C_3N_4 (002) is also found despite of its weak diffraction peak. No other impurity phase is detectable in patterns, suggesting the high purity of BC/CN heterostructure photocatalyst.

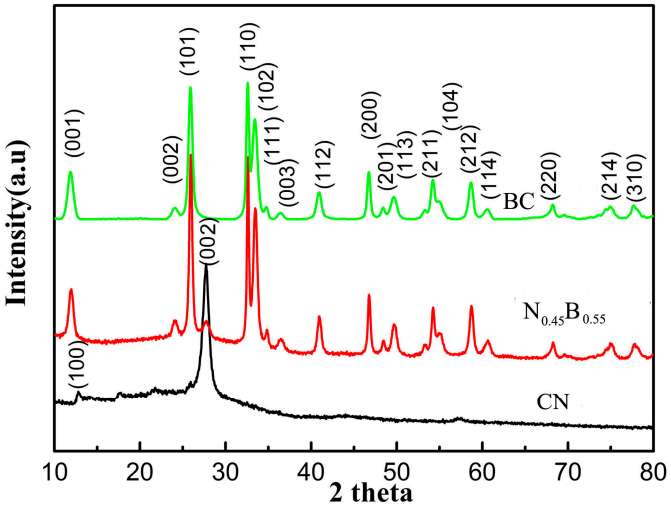

Figure 1. XRD patterns of the as-obtained BiOCl, g-C_3N_4, and $N_{0.45}B_{0.55}$ samples.

In this work, XPS analysis was conducted to further investigate the surface compositions and chemical status in the as-obtained g-C_3N_4, $N_{0.45}B_{0.55}$ and BiOCl samples. The results of binding energies spectra are shown in Figure 2. The survey spectra in Figure 2a show that the as-prepared $N_{0.45}B_{0.55}$ sample consists of C, N, O, Cl, and Bi. The high resolution spectra of C1s, N1s, O1s, Cl2p, and Bi 4f are shown in Figure 2b–f. In Figure 2b, we can find that C1s peak centered at about 284 eV can be assigned the adventitious carbon depositing on the samples in the measurement. As for bare g-C_3N_4, the major peak of C1s centered at about 287.4 eV is ascribed to the coordination between carbon atoms and three nitrogen atoms in the g-C_3N_4 lattice [50,51]. Simultaneously, in Figure 2c, the asymmetrical N1s peaks could be fitted into three peaks centered at 398.2 eV, 399.6 eV, and 400.2 eV, indicating that there probably exist three kinds of coordination related with N species in the g-C_3N_4 sample. According to previous literature [52], the peaks centered at about 398.4 eV and 399.7 eV are corresponding to the pyridinic-like (N-sp^2C) nitrogen and pyrrolic-like (N-sp^3C) nitrogen, respectively, whereas the peak with higher binding energy centered at about 400.2 eV corresponds to graphitic

nitrogen. Compared with those of pure g-C_3N_4, the C1s and N 1s peaks of $N_{0.45}B_{0.55}$ shift to higher binding energies by *ca*. 0.2 eV. The high resolution O1s spectrum of $N_{0.45}B_{0.55}$ shown in Figure 2d could be fitted well with two peaks centered at about 529.6 eV and 530.4 eV, relating to the lattice oxygen O^{2-} from a Bi-O bond and chemisorbed H_2O molecules or OH^- group on the surface, respectively [46], whereas these peaks in pure BiOCl shift to 529.3 eV and 530.1 eV. Two peaks with binding energies of 197.0 eV and 198.6 eV, corresponding to Cl 2p3/2 and Cl 2p1/2, respectively, are observed in the high resolution Cl 2p spectrum of $N_{0.45}B_{0.55}$ (Figure 2e), while these peaks in pure BiOCl shift to 197.7 eV and 199.2 eV. It can also be seen from Figure 2f that two strong peaks centered at 159.4 eV and 164.7 eV in $N_{0.45}B_{0.55}$ are attributed to Bi 4f5/2 and Bi 4f7/2, respectively, which are regarded as the characteristic of Bi^{3+} species in BiOCl network. Moreover, the peaks of Bi 4f5/2 and Bi 4f7/2 in pure BiOCl are also shifted up by 0.7 eV. Briefly, the above results indicate that both BiOCl and g-C_3N_4 with graphite-like sp^2-bonded structure exist in the heterostructure photocatalyst. Furthermore, the shifts of the peaks in the heterostructure photocatalyst, compared with those in the pure BiOCl and g-C_3N_4, are predominantly caused by the interaction between the BiOCl and g-C_3N_4 [53].

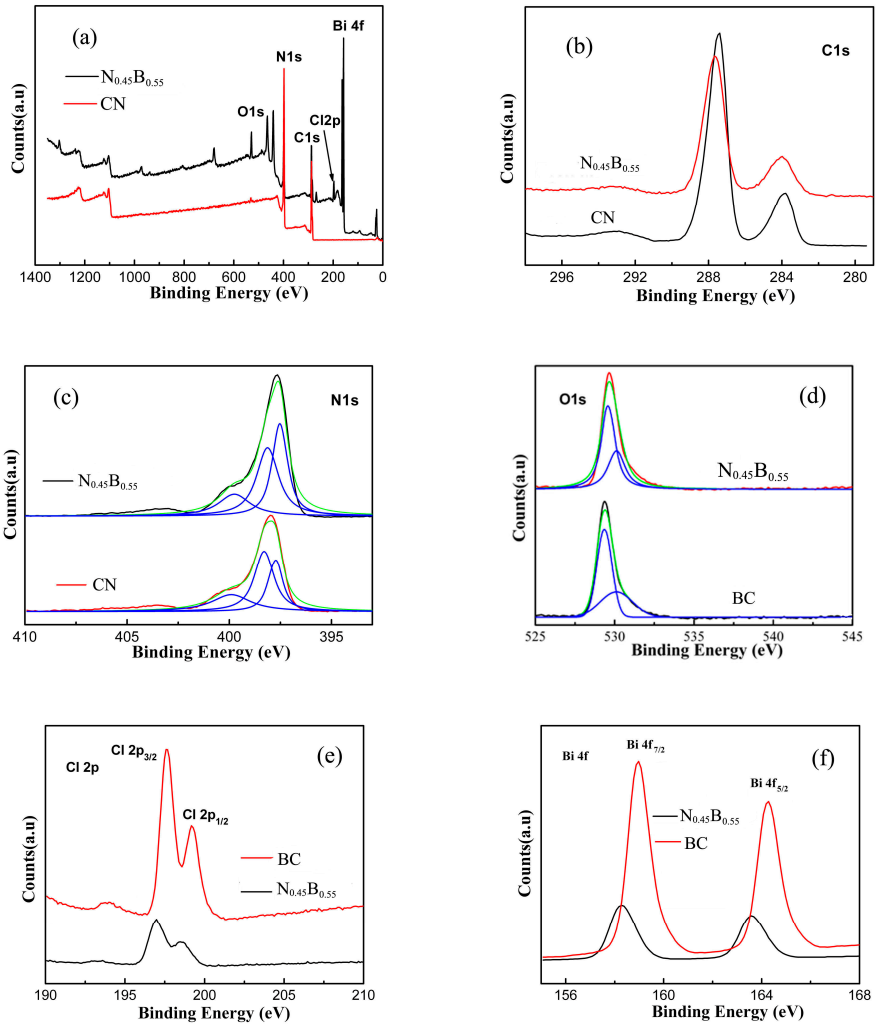

Figure 2. XPS spectra of the as-obtained BiOCl, g-C_3N_4 and $N_{0.45}B_{0.55}$ samples: (**a**) survey; (**b**) C1s; (**c**) N1s; (**d**) O1s; (**e**) Cl 2p; and (**f**) Bi 4f.

Figure 3 shows the FESEM images of the as-prepared pure g-C_3N_4, BiOCl, and $N_{0.45}B_{0.55}$ samples. In Figure 3a,b, numerous distorted nanosheets with coarse surface and ultrathin thickness are clearly observed in g-C_3N_4, indicating that the obtained g-C_3N_4 ultrathin nanosheets can be served as

a substrate for loading cocatalysts. As is seen in Figure 3c,d, pure BiOCl exhibits rose flower-like aggregate microstructure with sizes in the range of several nanometers to 1 μm, which are assembled with lots of nanoplates. Figure 3e shows hierarchical flower-like BiOCl nanoplates dispersing on the surface of g-C_3N_4 nanosheets. Furthermore, the detailed morphology and microstructure of the as-prepared bare g-C_3N_4, BiOCl, and $N_{0.45}B_{0.55}$ samples were examined by TEM and HRTEM, as shown in Figure 4. It is clear in Figure 4b that hierarchical flower-like BiOCl nanoplates anchored on the surface of g-C_3N_4 nanosheets discretely. Moreover, the magnified TEM image shown in the inset of Figure 4b indicates that BiOCl nanoplates were stacked and interconnected with each other randomly, the thickness of irregular plates were about 10 nm. Furthermore, the width and thickness of BiOCl seemingly decreased after being hybrid with g-C_3N_4. From the HRTEM image (Figure 4c), the interplanar lattice of 0.343 nm between adjacent lattice fringes of top surface in BiOCl can be indexed to (011) plane. Consulting previous study [54], the top and bottom surface are determined to be (001) facets. As indicated by HRTEM image (Figure 4d), a heterojunction was formed along the interface between BiOCl nanoplate and poorly crystallized g-C_3N_4 nanosheet, demonstrating that the two components are in close contact. Thereby, the large interface of 2D layered structure is constituted by (001) facets of BiOCl and (002) facets of g-C_3N_4, which favors the efficient transfer of photogenerated electron-hole pairs.

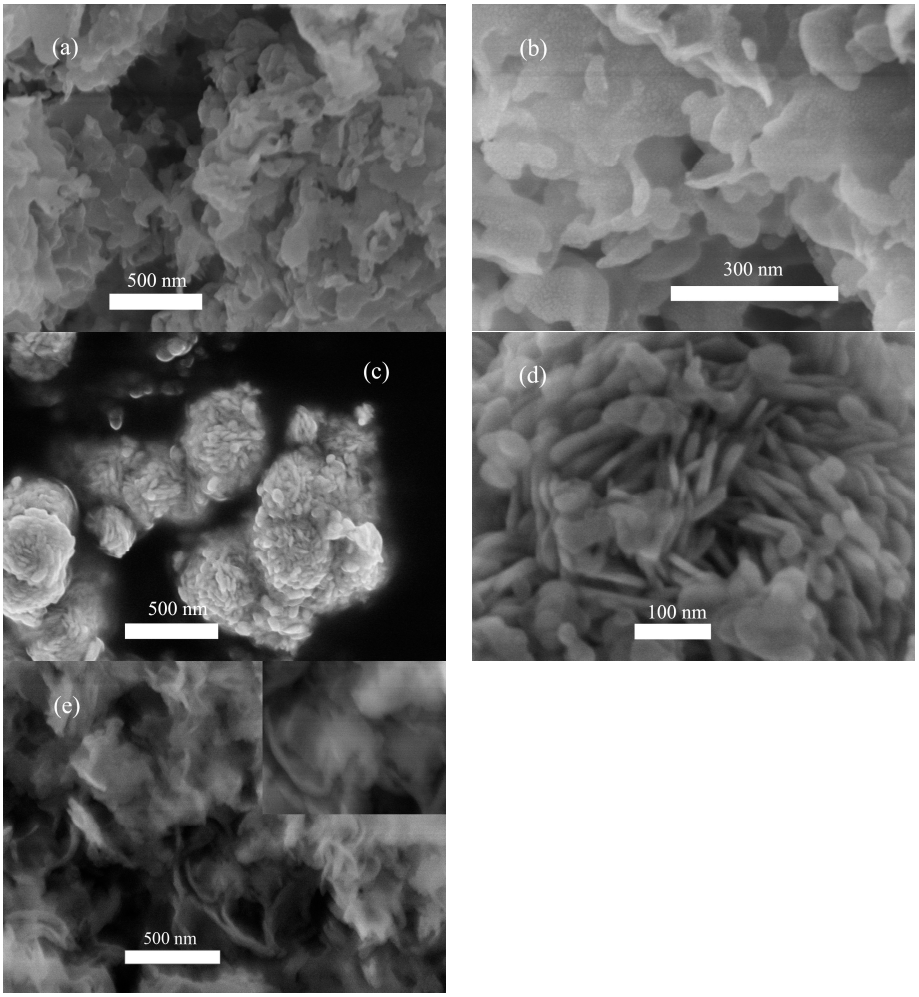

Figure 3. (**a**,**b**) Low and high magnification FESEM images of the as-obtained g-C_3N_4 sample; (**c**,**d**) low and high magnification FESEM images of the as-obtained BiOCl sample; and (**e**) high magnification FESEM image of $N_{0.45}B_{0.55}$ sample

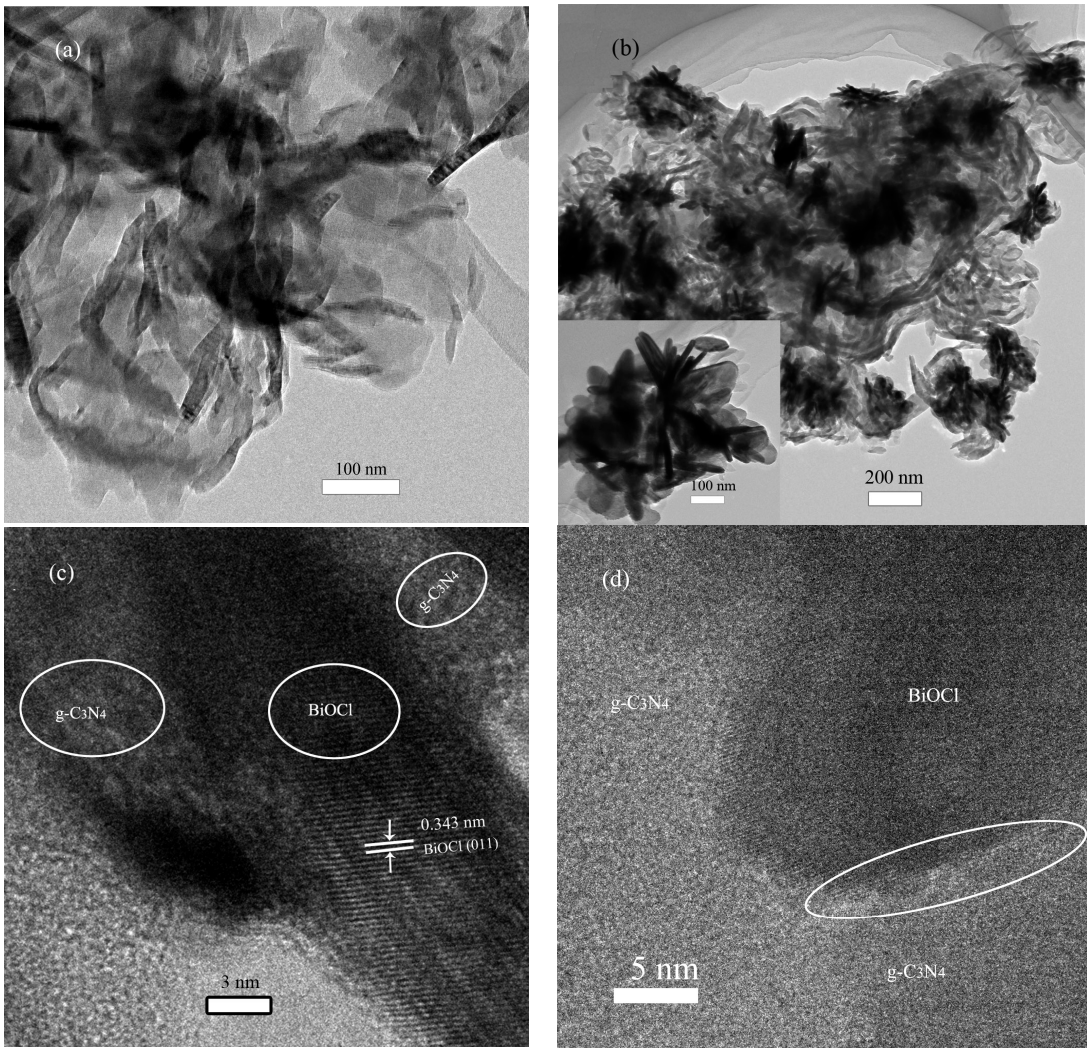

Figure 4. (**a**) TEM image of the as-obtained g-C_3N_4 sample; (**b**) TEM image of $N_{0.45}B_{0.55}$ sample; and (**c**,**d**) HRTEM images of $N_{0.45}B_{0.55}$ sample

2.2. BET Surface Area

The specific surface area of the as-prepared g-C_3N_4 and $N_{0.45}B_{0.55}$ samples was investigated by nitrogen adsorption-desorption isotherm analysis. Figure 5 depicts the nitrogen adsorption–desorption isotherms of pure g-C_3N_4 and $N_{0.45}B_{0.55}$ samples. The isotherms of g-C_3N_4 and $N_{0.45}B_{0.55}$ are similar and both of them can be characterized as classical type IV, revealing the nature of mesoporous materials [55]. The hysteresis loops can be categorized as typical H3 hysteresis loop for the relative pressure P/P_0 in the range of 0.7–1. According to Brunauer-Emmett-Teller method, the specific surface areas of g-C_3N_4 and $N_{0.45}B_{0.55}$ are calculated to be 95.5 m^2/g and 44.2 m^2/g, respectively. The BET surface area of the $N_{0.45}B_{0.55}$ nanocomposites decreases in comparison with pure g-C_3N_4, however, the $N_{0.45}B_{0.55}$ nanocomposites still have larger surface area and porous structure, which could contribute to the enhanced visible-light photocatalytic performance.

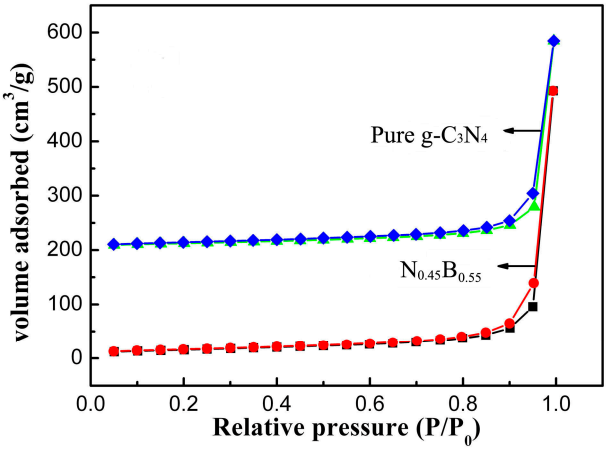

Figure 5. Nitrogen adsorption-desorption isotherms of the as-obtained g-C_3N_4 and $N_{0.45}B_{0.55}$ samples.

2.3. Optical and Electronic Properties

Figure 6 shows the optical absorption properties of the as-prepared samples, which were measured by using the UV-vis diffuse reflectance spectra (DRS). As is evident in Figure 6, the optical absorption band of pure BiOCl presents a steep absorption edge in the UV region of 368 nm, agreeing well with previous reports [12,13]. Compared with pure BiOCl, the $N_{0.45}B_{0.55}$ nanocomposites extend their light absorption to visible light region. That is to say, after being coupled with g-C_3N_4, $N_{0.45}B_{0.55}$ nanocomposites exhibit enhanced visible light absorption ability owing to the fact that the heterostructure formed between BiOCl and g-C_3N_4 changes the optical properties of the photocatalysts. Based on absorption results above, the optimal bandgap energy (Eg) of a semiconductor can be determined from the well-known equation: $A(h\nu\text{-}E_g)^n = \alpha h\nu$, where α, A, and $h\nu$ represent the adsorption coefficient, proportionality and photon energy, while the value of n is dependent on the intrinsic characteristic of semiconductor, $n = 2$ for an indirect transition semiconductor and $n = 1/2$ for a direct transition semiconductor [56]. For both g-C_3N_4 and BiOCl, the value of n is equal to 2. By extrapolating the linear portion of $h\nu$ against $(\alpha h\nu)^{1/2}$ curves, the band gaps of BiOCl and g-C_3N_4 are estimated to be about 3.3 eV and 2.6 eV, respectively.

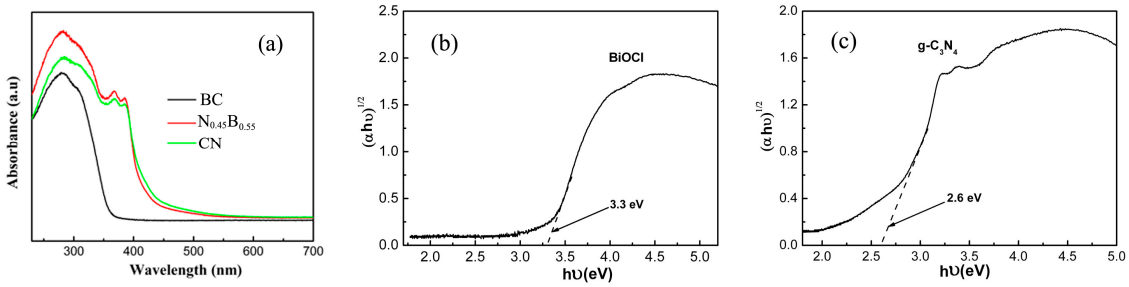

Figure 6. (**a**) UV-vis diffuse reflectance spectra of BiOCl, g-C_3N_4, and $N_{0.45}B_{0.55}$ samples; (**b**) the corresponding $(\alpha h\nu)^{1/2}$ vs. photon energy ($h\nu$) plot of BiOCl sample; and (**c**) the corresponding $(\alpha h\nu)^2$ vs. photon energy ($h\nu$) plot of bare g-C_3N_4 sample.

It is vital to investigate the transportation and recombination of processes of photo-induced electron-hole pairs for exploring the main cause of the enhanced photocatalytic activity. As is well known, PL spectra of the as-prepared samples are valuable to explain the migration and recombination processes of photo-induced electron-hole pairs. After being activated by the light, photocatalysts can generate electrons and holes, while the photoinduced holes and electrons recombine together, resulting in the energy release in the form of fluorescence emission. Accordingly, it can be

inferred that lower fluorescence emission intensity indicates lower recombination rate of electron-hole. The fluorescence emission spectra of the as-prepared photocatalysts excited at a wavelength of 310 nm are shown in Figure 7a. All of photocatalysts exhibit a broad emission peak centered at about 480 nm, which could be ascribed to the band-band PL phenomenon of the photo-induced charge carriers for g-C_3N_4. Bare g-C_3N_4 exhibits the highest PL emission intensity among these photocatalysts, indicating that the charge carrier recombination in bare g-C_3N_4 is the fastest of all photocatalysts. The $N_{0.45}B_{0.55}$ nanocomposites exhibit the lowest PL emission intensity, indicating that the recombination of photo-generated charge carriers is suppressed and the efficient separation of photo-generated charge carriers is successfully achieved. The photoluminescence decay kinetics was further investigated by time-resolved spectra. As shown in Figure 7b, the $N_{0.45}B_{0.55}$ nanocomposites have the longer lifetime corresponding to the slower charge recombination of the excited state in comparison with g-C_3N_4. According to previous study [57], the average decay lifetimes of carriers in the sample the $N_{0.45}B_{0.55}$ nanocomposites and g-C_3N_4 were estimated to be about 3.47 ns and 0.42 ns, respectively. The significantly prolonged life time of the charge carriers indicates that a lower recombination and a higher separation of charge carriers exist in the $N_{0.45}B_{0.55}$ nanocomposites catalyst. Thus, the high separation efficiency can enhance the probability of their involvement in the photocatalytic reaction before recombination, hence improving the photoactivity.

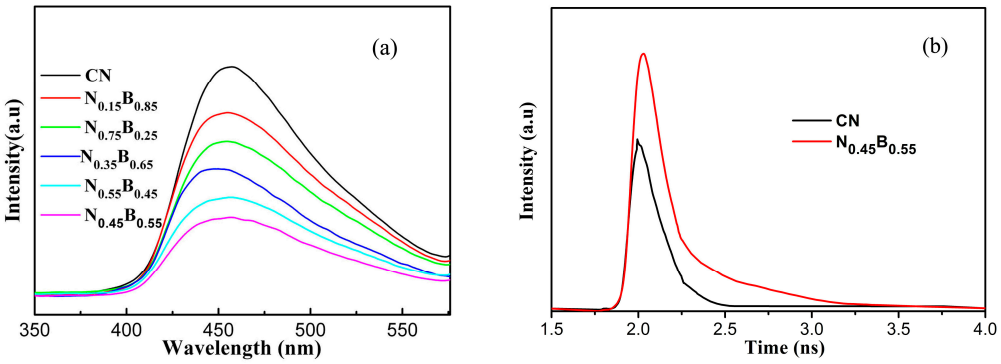

Figure 7. (**a**) PL spectra of g-C_3N_4 and BC/CN nanocomposites; and (**b**) time-resolved photoluminescence spectra monitored at 480 nm of g-C_3N_4 and $N_{0.45}B_{0.55}$ samples

2.4. Photocatalytic Performance

To evaluate the photoactivity of the as-prepared BiOCl, g-C_3N_4 and CN-BC nanocomposites, the photodegradation of MB in water was investigated under visible light irradiation in this work. The changes in the characteristic absorption band of MB at 662 nm were used to monitor the photocatalytic performance. The photodegradation efficiency (%) of MB was expressed by C_t/C_0, in which C_t represents concentration of the MB solution at a certain irradiation time t, while C_0 is the initial concentration of MB solution after adsorption–desorption equilibrium. For comparison, the photocatalytic reactions induced by different photocatalysts were carried out with otherwise identical conditions under visible light irradiation.

Figure 8a illustrates the time-dependent absorption spectra of MB aqueous solution degraded by $N_{0.45}B_{0.55}$ nanocomposites under visible light irradiation. As shown in Figure 8a, the intensity of the characteristic peak decreased very quickly with the irradiation time prolonging. Correspondingly, the color of the suspension gradually becomes lighter. Figure 8b illustrates the effects of the amount of g-C_3N_4 on the photocatalytic degradation of MB solution. As shown in Figure 8b, pure BiOCl and g-C_3N_4 exhibited generally low photocatalytic performance. After being irradiated for 30 min, only about 56% and 69% of MB can be degraded by bare BiOCl and g-C_3N_4, respectively. As for BiOCl, the photodegradation of MB under visible light irradiation could be ascribed to the indirect dye photosensitization procedure. The above low photocatalytic performance is most likely related with the intrinsic spectral response

and fast recombination rate of photogenerated electron-hole pairs. Comparably, the as-prepared CN-BC nanocomposites showed higher photocatalytic performance under visible light irradiation than BiOCl and g-C_3N_4. Among these nanocomposites, $N_{0.45}B_{0.55}$ nanocomposites have the highest photocatalytic efficiency, and an almost complete photodegradation of MB was achieved after visible light irradiation for 30 min. Thus, it can be inferred that the optimum amount of loaded g-C_3N_4 nanosheets is 45%. When the content of loaded g-C_3N_4 nanosheets in CN-BC nanocomposites increases higher than the optimal amount, the photocatalytic performance decreases contrarily. The above result indicates that the mass ratio of g-C_3N_4 in the as-prepared nanocomposites is crucial to the synergistic effect during the photodegradation process [58]. In order to quantitate the MB photodegradation rate, the reaction kinetics curves is approximated as a pseudo-first-order process by linear transforms $\ln(C_0/C_t) = kt$, where C_t and C_0 represent MB concentration at time t (min) and t = 0; k (min^{-1}) is the photodegradation reaction rate constant. The corresponding kinetic constant (k) for MB photodegradation over different photocatalysts is shown in Figure 8c. The rate constant (k) of the MB photodegradation over $N_{0.45}B_{0.55}$ was estimated to be *ca*. 0.157 min^{-1}, which was about four times higher than those over BiOCl (0.0275 min^{-1}) or g-C_3N_4 (0.0393 min^{-1}).

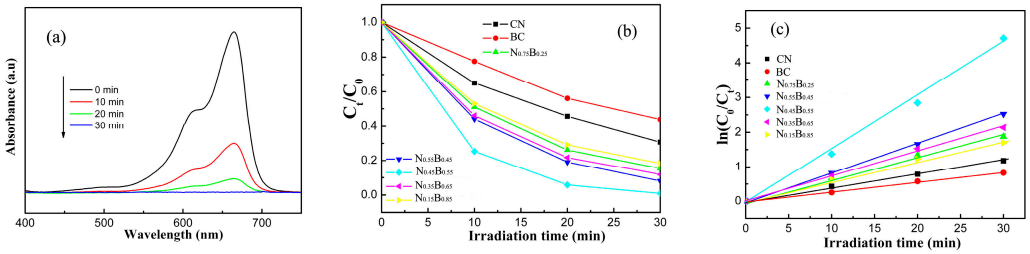

Figure 8. (**a**) Time-dependent absorption spectra of MB aqueous solution degraded by $N_{0.45}B_{0.55}$ nanocomposites under visible light irradiation; (**b**) Photocatalytic degradation curves; and (**c**) photodegradation kinetics of MB in presence of different photocatalysts under visible light irradiation.

2.5. Catalyst Photostability and Photocatalytic Mechanism

Photostability is one of the significant properties for an excellent photocatalyst. Thus, the repeatability experiments of MB degradation over the $N_{0.45}B_{0.55}$ photocatalyst were performed to evaluate the reusability and stability, and the results are shown in Figure 9. It is very clear in Figure 9 that the degradation degree is approximate to 99% after the fifth cycling run, indicating that the $N_{0.45}B_{0.55}$ photocatalyst exhibits adequate photostability for degrading MB pollutant.

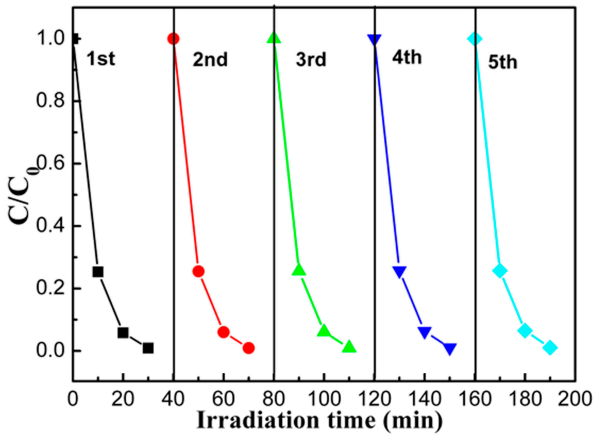

Figure 9. Cycling runs in the photocatalytic degradation of MB in the presence of $N_{0.45}B_{0.55}$ sample.

It is essential to investigate the proposed mechanism for a heterostructure photocatalyst system. In the photocatalytic degradation process of the pollutants, some reactive species, such as •OH, $\bullet O_2^-$, and h^+, are available for involving oxidation-reduction reactions. To evaluate the effect of the above species on the degradation process, different scavenges of EDTA disodium (Na_2-EDTA 4 mmol L^{-1}), methanol (ME 2 mmol L^{-1}), and benzoquinone (BQ 2 mmol L^{-1}) were employed to capture h^+, •OH, and $\bullet O_2^-$, respectively. Figure 10 shows the effect of various scavengers on the visible light photocatalytic performance of $N_{0.45}B_{0.55}$ toward the degradation of MB. Compared with scavenger-free $N_{0.45}B_{0.55}$ photocatalytic system, the degradation rate of MB exhibited a slight decrease after the addition of ME (2 mmol L^{-1}) or BQ (2 mmol L^{-1}) in the reaction system. On the contrary, the photocatalytic performance of $N_{0.45}B_{0.55}$ was significantly suppressed upon the introduction of Na_2-EDTA (4 mmol L^{-1}) to the above system, indicating that the photo-generated holes separated in the heterostructure contribute overwhelmingly to the highly enhanced photocatalytic performance.

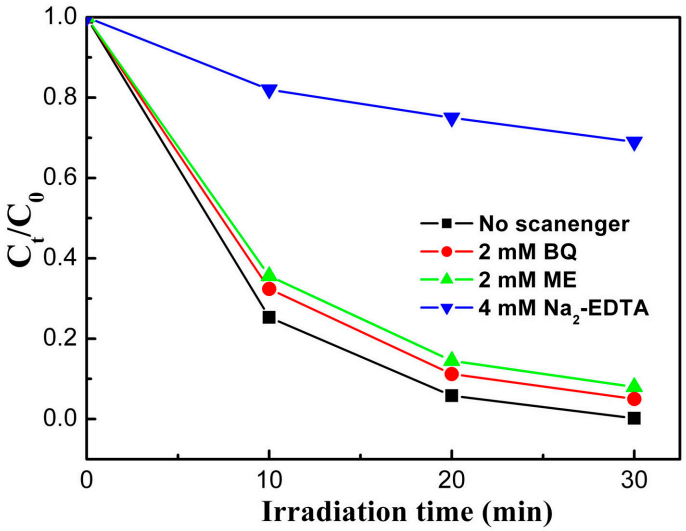

Figure 10. Effect of various scavengers on the visible light photocatalytic performance of $N_{0.45}B_{0.55}$ sample toward the degradation of MB.

As is well known, the p-n heterostructure in a photocatalytic system plays a great role in accelerating the efficient separation of photogenerated electron–hole pairs and enhancing the photocatalytic activity [46–49]. Theoretically, adequate amounts of p-n heterojunctions between (001) facets of BiOCl and (002) facets of g-C_3N_4 are formed during the synthetic process, which facilitates electrons from the n-type C_3N_4 in the heterostructure interfaces transferring to the p-type BiOCl. Actually, the holes are inclined to stay at lower energy states, leading to the fact that the status of positively charged holes in the p-type BiOCl and extra negatively charged electrons in the n-type C_3N_4 will be achieved [59]. Consequently, an internal electric field is simultaneously formed with a positively charged portion at the interface of p-type BiOCl nanoplates and a negatively charged portion at the interface of n-type g-C_3N_4 nanosheets, and the direction of the internal electric field is from n-type g-C_3N_4 to p-type BiOCl. Additionally, the photocatalytic performance of BC/CN nanocomposites is closely related with the band structure. The potentials of the valence band (VB) and conduction band (CB) of the two semiconductors at the point of zero charge can be calculated according to the two equations as follows:

$$E_{CB} = X - E^e - 0.5E_g \quad (1)$$

$$E_{VB} = E_{CB} + E_g \quad (2)$$

where X, E_e and E_g represent the absolute electronegativity of the corresponding semiconductor, the energy of free electrons on the hydrogen scale (4.5 eV) and band gap of the corresponding

semiconductor, respectively. The X values of BiOCl and g-C_3N_4 are calculated to be 6.33 eV and 4.72 eV, respectively. Through theoretical calculation, the CB potentials and VB potentials for BiOCl and g-C_3N_4 are estimated to be about 0.18 eV and 3.48 eV, and −1.08 eV and 1.52 eV, respectively. Under visible-light irradiation, photogenerated electron-hole pairs in g-C_3N_4 are obtained due to its narrow bandgap. Afterwards, the electrons in the CB region of the n-type g-C_3N_4 can easily transfer to the p-type BiOCl due to the well-matched band structure and closely contacted interface, and the holes in the VB region of the n-type BiOCl transfer to the p-type g-C_3N_4 contrarily. Furthermore, the formation model for the heterostructure photocatalyst and the schematic drawing of electron–hole separation process is illustrated in Figure 11 on the basis of the analysis mentioned above. Therefore, it can be inferred that an effective separation of photogenerated electron–hole pairs in heterostructure photocatalyst are mainly ascribed to the inner electric field assisted charge transfer at the junction interfaces constituted by (001) facets of BiOCl and (002) facets of g-C_3N_4.

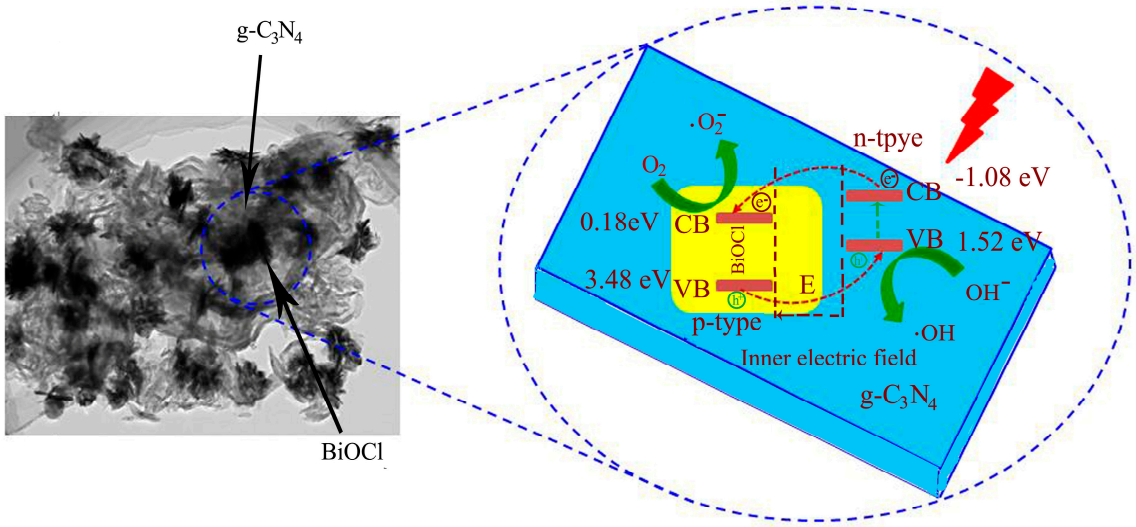

Figure 11. Schematic illustration of the charge transfer process over g-C_3N_4/BiOCl heterostructure.

3. Experimental Section

3.1. Materials

All the chemicals, including urea ($(NH_2)_2CO$), bismuth nitrate pentahydrate ($Bi(NO_3)_3{\cdot}5H_2O$), potassium choloride (KCl), methylene blue (MB), ethylene glycol, glycerine and ethanol were purchased from Sinopharm Chemical Reagent CO., Ltd., Shanghai, China. All of them were of analytical grade, and used as received without further purification. Deionized water was used throughout the study.

3.2. Synthesis of g-C_3N_4/ BiOCl Heterostructure

3.2.1. Synthesis of Ultrathin g-C_3N_4 Nanosheets

Ultrathin g-C_3N_4 nanosheets were prepared by a one-step polymerization method, which was similar to the previous report [22]. In detail, 20 g urea powder was put into an alumina crucible with a cover in air. Subsequently, the crucible containing 20 g urea powder was heated in a muffle furnace at 580 °C for 3 h with a heating rate of 3 °C /min. The obtained product was washed with dilute hydrochloric acid (0.1 M), deionized water and ethanol to remove any residual species adsorbed on the surface, followed by drying at 60 °C for 12 h.

3.2.2. Synthesis of g-C_3N_4 /BiOCl Heterostructure

The typical preparation of BC/CN was carried out through hydrolysis of bismuth salt in ethylene glycol solvent. First, 2 mmol of $Bi(NO_3)_3 \cdot 5H_2O$ was added to 100 mL mixed solvents (containing 80 mL ethylene glycol and 20 mL glycerine) and stirred for 20 min to form a transparent solution, and then a certain amount of g-C_3N_4 nanosheets was completely dispersed into the above solution under vigorous magnetic stirring. After that, 2 mmol of KCl was added to the mixture solution and stirred for 1 h to obtain a stable and homogeneous suspension. Subsequently, 50 mL deionized water was slowly dropped into the above suspension under vigorous magnetic stirring. The mixture was then stirred for 3 h at room temperature to make the hydrolysis reaction complete. Finally, the obtained precipitate was collected, centrifuged, and washed with distilled water and ethanol, respectively, followed by drying at 60 °C for 12 h. A series of BC/CN heterostructure photocatalysts with different ratio of 0.15:0.85, 0.35:0.65, 0.45:0.55, 0.55:0.45, and 0.75:0.25 was prepared via the similar synthetic process. Briefly, the as-obtained BC/CN heterostructure photocatalysts were denoted as $N_{0.15}B_{0.85}$, $N_{0.35}B_{0.65}$, $N_{0.45}B_{0.55}$, $N_{0.55}B_{0.45}$, and $N_{0.25}B_{0.75}$, respectively. For comparison, bare BiOCl was also prepared via the similar procedure when no g-C_3N_4 nanosheets were added.

3.3. Characterization

Crystal structure identification was carried out on a Bruker D8 (Bruker, Billerica, MA, USA) advance X-ray diffractometer (XRD) equipped with Cu Kα radiation (λ = 0.15406 nm) at 40 kV and 40 mA over the 2θ range of 10°–80°. X-ray photoelectron spectroscopy (XPS) analysis was conducted on an ESCALAB 250Xi spectrometer (Thermo Fisher Scientific, NewYork, NY, USA) equipped with monochromatized Al-Kα radiation, and the binding energy positions were calibrated against the C1s at 284.6 eV. The morphologies of the as-prepared BC/CN heterostructure photocatalysts were observed by a Hitachi S-4800 field emission scanning electron microscope (Hitachi, Toyko, Japan) and a JEM 2100F microscope (JEOL Ltd., Tokyo, Japan) with a field gun, operated at an acceleration voltage of 200 kV, respectively. The Brunauer-Emmett-Teller (BET) specific surface area of the as-prepared BC/CN heterostructure photocatalysts was evaluated based on nitrogen adsorption and desorption isotherms at 77 K using a Quantachrome NOVA 2000e sorption analyzer (Quantachrome Instruments, Boynton Beach, FL, USA). Using $BaSO_4$ as the reference, UV-vis diffuse reflectance spectra were measured by a UV-vis spectrophotometer (TU 1901, Puxi, Beijing, China). Photoluminescence (PL) spectra of the as-prepared products were recorded on a Hitachi F-4500 fluorescence spectrophotometer (Hitachi, Toyko, Japan) using an excitation wavelength of 310 nm. Time-resolved fluorescence measurement of the as-prepared samples was conducted on a fluorescence spectrophotometer (Horiba Fluorolog 3-22, JY Horiba, Madison, WI, USA).

3.4. Photocatalytic Experiments

The visible-light photocatalytic performance of the as-prepared samples was evaluated by the degradation of MB aqueous solution under visible-light irradiation. As reported in the previous work [32,60,61], 60 mL MB aqueous solution (1.0×10^{-5} M) was added into a culture dish with a diameter of 70 mm which was coated with 80 mg prepared catalyst on the surface. Two daylight lamps (60 W, $\lambda \geq 400$ nm) were used as a light source to trigger the photocatalytic reaction. The two lamps was placed parallel and hung vertically above the culture dish, and the distance between the dish and the lamps was about 10 cm. The average light intensity striking the surface of the reaction solution was about 20 mW/cm^2. Prior to light illumination, the solution was allowed to reach an adsorption-desorption equilibrium among the catalyst, MB and water. At given irradiating time intervals, 5 mL reacted solution was taken from the suspension, and then was centrifuged for the concentration measurement. The concentration of MB aqueous solution was determined by using an UV-vis spectrophotometer (TU 1901, Puxi, Beijing, China) at its maximum absorbance wavelength (662 nm).

4. Conclusions

In summary, the novel p-n heterostructure photocatalyst of BC/CN was successfully synthesized via a thermal polymerization of urea precursor followed by hydrolysis route. Compared with pure g-C_3N_4 and BiOCl, the BC/CN heterostructures exhibit high photocatalytic efficiency. The effective separation of photo-generated electron and the intimately contacted large interfaces between g-C_3N_4 and BiOCl are the main causes for the enhancement of photocatalytic performance, according to energy band theory and the formation of an internal electrostatic field. This study provides a simple and economical strategy for the design and development of high-efficiency visible-light-driven p-n heterostructure photocatalysts for the applications in environmental remediation and clean energy production.

Acknowledgments: The authors express their grateful thanks to the National Natural Science Foundation of China (Grant U1304520), Education Department of Henan Province for the fund support (18A 430020), and Hubei Provincial Natural Science Foundation (2016CFB337). We also express our thanks to Xiaoqing Liu from Wuhan University of Technology for assistance with the HRTEM characterizations.

Author Contributions: Tiekun Jia conceived and designed the experiments; Jili Li, Fang Fu and Ying Zhang performed the synthetic experiment; Junwei Zhao and Xiaohui Wang performed the photo-catalytic activity of the as-prepared samples; Fei Long gave basic and important ideas as well as precise instruction; Zhao Deng analyzed the data; and Tiekun Jia wrote the paper.

Conflicts of Interest: The authors declared that we do not have any direct financial relation with the commercial identities mentioned in this paper that might lead to any conflict of interest for any of the authors.

Abbreviations

The following abbreviations are used in this manuscript

XRD	X-ray diffraction
SEM	Scanning electron microscopy
TEM	Transmission electron microscopy
HRTEM	High resolution transmission electron microscopy
XPS	X-ray photoelectron spectroscopy
BET	Brunauer–Emmett–Teller
DRS	Diffuse reflectance spectrum
PL	Photoluminescence
MB	Methylene blue

References

1. Liu, S.W.; Yu, J.G.; Jaroniec, M. Tuable photocatalytic selectivity of hollow TiO_2 microspheres composed of anatase polyhedra with exposed {001} facets. *J. Am. Chem. Soc.* **2010**, *132*, 11914–11916. [CrossRef] [PubMed]
2. Zheng, Z.Y.; Wang, Z.F.; Xie, L.Y.; Fang, Z.B.; Feng, W.H.; Huang, M.L.; Liu, P. Synthesis of single-crystal-like TiO_2 hierarchical spheres with exposed {101} and {111} facets via lysine-inspired method. *Appl. Surf. Sci.* **2015**, *353*, 714–722. [CrossRef]
3. Vinu, R.; Madras, G. Kinetics of simultaneous photocatalytic degradation of phenolic compounds and reduction of metal ions with nano-TiO_2. *Environ. Sci. Technol.* **2008**, *42*, 913–919. [CrossRef] [PubMed]
4. Li, G.; Liu, J.; Lan, J.; Li, G.; Chen, Q.; Jiang, G. 3D hierarchical anatase TiO_2 superstructures constructed by "nanobricks" built nanosheets with exposed{001}facets: Facile synthesis, formation mechanism and superior photocatalyticactivity. *CrystEngComm* **2014**, *16*, 10547–10552. [CrossRef]
5. Zhu, X.F.; Cheng, B.; Yu, J.G.; Ho, W.K. Halogen poisoning effect of Pt-TiO_2 for formaldehyde catalytic oxidation performance at room temperature. *Appl. Surf. Sci.* **2016**, *364*, 808–814. [CrossRef]
6. Cheng, H.F.; Huang, B.B.; Dai, Y. Engineering BiOX (X = Cl, Br, I) nanostructures for highly efficient photocatalytic applications. *Nanoscale* **2014**, *6*, 2009–2026. [CrossRef] [PubMed]
7. Wu, S.J.; Wang, C.; Cui, Y.F. Controllable growth of BiOCl film with high percentage of exposed {001} facets. *Appl. Surf. Sci.* **2014**, *289*, 266–273. [CrossRef]

8. Guan, L.M.; Xiao, C.; Zhang, J.; Fan, S.J.; An, R.; Cheng, Q.M.; Xie, J.F.; Zhou, M.; Ye, B.J.; Xie, Y. Vacancy associates promoting solar-driven photocatalytic activity of ultrathin bismuth oxychloride microspheres in degradation of bisphenol A. *Environ. Sci. Technol.* **2015**, *49*, 6240–6248.
9. Liu, W.W.; Shang, Y.Y.; Zhu, A.Q.; Tan, P.F.; Liu, Y.; Qiao, L.L.; Chu, D.W.; Xiong, X.; Pan, J. Enhanced performance of doped BiOCl nanoplates for photocatalysis: Understanding from doping insight into improved spatial carrier separation. *J. Mater. Chem. A* **2017**, *5*, 12542–12549. [CrossRef]
10. Chen, L.; Yin, S.-F.; Huang, R.; Zhou, Y.; Luo, S.-L.; Au, C.-T. Facile synthesis of BiOCl nano-flowers of narrow band gap and their visible-light-induced photocatalytic property. *Catal. Commun.* **2012**, *23*, 54–57. [CrossRef]
11. Jiang, J.; Zhao, K.; Xiao, X.Y.; Zhang, L.Z. Synthesis and faceted-dependent photoreactivity of BiOCl single-crystalline nanosheets. *J. Am. Chem. Soc.* **2012**, *134*, 4473–4476. [CrossRef] [PubMed]
12. Shenawi-Khalil, S.; Uvarov, V.; Menes, E.; Popov, I.; Sasson, Y. New efficient visible light photocatalyst based on heterojunction of BiOCl-bismuth oxyhydrate. *Appl. Catal. A* **2012**, *413*, 1–9. [CrossRef]
13. Cao, J.; Xu, B.Y.; Lin, H.L.; Luo, B.D.; Chen, S.F. Novel Bi_2S_3-sensitized BiOCl with highly visisible light photocatalytic activity for the removal of rhodamine B. *Catal. Commun.* **2012**, *26*, 204–208. [CrossRef]
14. Cao, Q.W.; Zheng, Y.F.; Song, X.C. The enhanced visible light photocatalytic activity of $Bi_2W_xMo_{1-x}O_6$-BiOCl heterojunctions with adjustable energy band. *Ceram. Int.* **2016**, *42*, 14533–14542. [CrossRef]
15. Xiao, X.R.; Liang, H.; Zuo, M.X.; Nan, J.; Li, L.; Zhang, W. One-pot solvothermal synthesis of three-dimensional (3D) BiOI/BiOCl composites with enhanced visible-light photocatalytic activities for the degradation of bisphenol-A. *J. Hazard. Mater.* **2012**, *233–234*, 122–130. [CrossRef] [PubMed]
16. He, Z.; Shi, Y.; Gao, C.; Wen, L.; Chen, J.; Song, S. BiOCl/$BiVO_4$ p–n heterojunction with enhanced photocatalytic activity under visible-light irradiation. *J. Phys. Chem. C* **2014**, *118*, 389–398. [CrossRef]
17. Shamaila, S.; Sajjad, A.K.; Chen, F.; Zhang, J. WO_3/BiOCl, a novel heterojunction as visible light photocatalyst. *J. Colloid Interface Sci.* **2011**, *356*, 465–472. [CrossRef] [PubMed]
18. Lu, H.; Xu, L.; Wei, B.; Zhang, M.; Gao, H.; Sun, W. Enhanced photosensitization process induced by the p–n junction of $Bi_2O_2CO_3$/BiOCl heterojunctions on the degradation of rhodamine B. *Appl. Surf. Sci.* **2014**, *303*, 360–366. [CrossRef]
19. Chai, S.Y.; Kim, Y.J.; Jung, M.H.; Chakraborty, A.K.; Jung, D.; Lee, W.L. Heterojunctioned BiOCl/Bi_2O_3, a new visible light photocatalyst. *J. Catal.* **2009**, *262*, 144–149. [CrossRef]
20. Cao, S.W.; Low, X.J.; Yu, J.G.; Jaroniec, M. Polymeric photocatalysts based on graphitic carbon nitride. *Adv. Mater.* **2015**, *27*, 2150–2176. [CrossRef] [PubMed]
21. Wang, Y.; Wang, X.; Antonietti, M. Polymeric Graphitic carbon nitride as a heterogeneous organocatalyst: From photochemistry to multipurpose catalysis to sustainable chemistry. *Angew. Chem.* **2012**, *51*, 68–89. [CrossRef] [PubMed]
22. Xu, J.; Zhang, L.W.; Shi, R.; Zhu, Y.F. Chemical exfoliation of graphitic carbon nitride for efficient heterogeneous photocatalysis. *J. Mater. Chem. A* **2013**, *1*, 14766–14772. [CrossRef]
23. Liu, J.H.; Zhang, T.K.; Wang, Z.C.; Dawson, G.; Chen, W. Simple pyrolysis of urea into graphitic carbon nitride with recyclable adsorption and photocatalytic activity. *J. Mater. Chem.* **2011**, *21*, 14398–14401. [CrossRef]
24. Yu, Y.Z.; Wang, J.G. Direct microwave synthesis of graphitic C_3N_4 with improved visible-light photocatalytic activity. *Ceram. Int.* **2016**, *42*, 4063–4071. [CrossRef]
25. Xiang, Q.; Yu, J.; Jaroniec, M. Preparation and enhanced visible-Light photocatalytic H_2-production activity of graphene/C_3N_4 composites. *J. Phys. Chem. C* **2011**, *115*, 7355–7363. [CrossRef]
26. Groenewolt, M.; Antonietti, M. Synthesis of g-C_3N_4 nanoparticles in mesoporous silica host matrices. *Adv. Mater.* **2005**, *17*, 1789–1792. [CrossRef]
27. Chen, W.; Liu, T.Y.; Huang, T.; Liu, X.H.; Zhu, J.W.; Duan, G.R.; Yang, X.J. In situ fabrication of novel Z-scheme Bi_2WO_6 quantum dots/g-C_3N_4 ultrathin nanosheets heterostructures with improved photocatalytic activity. *Appl. Surf. Sci.* **2015**, *355*, 379–387. [CrossRef]
28. Zhao, W.; Wei, Z.B.; He, H.; Xu, J.; Li, J.H.; Yang, S.G.; Sun, C. Supporting 1-D $AgVO_3$ nanoribbons on single layer 2-D graphitic carbon nitride ultrathin nanosheets and their excellent photocatalytic activities. *Appl. Catal. A Gen.* **2015**, *501*, 74–82. [CrossRef]

29. Li, Z.; Yang, S.; Zhou, J.; Li, D.; Zhou, X.; Ge, C.; Fang, Y. Novel mesoporous g-C_3N_4 and $BiPO_4$ nanorods hybrid architectures and their enhanced visible-light driven photocatalytic performances. *Chem. Eng. J.* **2014**, *241*, 344–351. [CrossRef]
30. Yao, Y.J.; Lu, F.; Zhu, Y.P.; Wei, F.Y.; Liu, X.T.; Lian, C.; Wang, S.B. Magnetic core-shell $CuFe_2O_4$@C_3N_4 hybrids for visible light photocatalysis of Orange II. *J. Hazard. Mater.* **2015**, *297*, 224–233. [CrossRef] [PubMed]
31. Sun, M.; Yan, Q.; Yan, T.; Li, M.M.; Wei, D.; Wang, Z.P.; Wei, Q.; Du, B. Facile fabrication of 3D flower-like heterostructured g-C_3N_4/SnS_2 composite with efficient photocatalytic activity under visible light. *RSC Adv.* **2014**, *4*, 31019–31027. [CrossRef]
32. Zhang, F.; Xie, F.; Zhu, S.; Liu, J.; Zhang, J.; Mei, S.; Zhao, W. A novel photofunctional g-C_3N_4/Ag_3PO_4 bulk heterojunction for decolorization of RhB. *Chem. Eng. J.* **2013**, *228*, 435–441. [CrossRef]
33. Chen, J.; Shen, S.H.; Guo, P.H.; Wang, M.; Wu, P.; Wang, X.X.; Guo, L.J. In-situ reduction synthesis of nano-sized Cu_2O particles modifyingg-C_3N_4 for enhanced photocatalytic hydrogen production. *Appl. Catal. B Environ.* **2014**, *152–153*, 335–341. [CrossRef]
34. Zhang, X.; Hu, J.; Jiang, H. Facile modification of a graphitic carbon nitride catalyst to improve its photo-reactivity under visible light irradiation. *Chem. Eng. J.* **2014**, *256*, 230–237. [CrossRef]
35. Zhang, L.H.; Li, L.; Sun, X.M.; Liu, P.; Yang, D.F.; Zhao, X.S. ZnO-Layered double hydroxide@graphitic carbon nitride composite for consecutive adsorption and photodegradation of dyes under UV and visible lights. *Materials* **2016**, *9*, 927. [CrossRef] [PubMed]
36. Leong, K.H.; Liu, S.L.; Sim, L.C.; Saravanana, P.; Jang, M.; Ibrahim, S. Surface reconstruction of titania with g-C_3N_4 and Ag for promoting efficient electrons migration and enhanced visible light photocatalysis. *Appl. Surf. Sci.* **2015**, *358*, 370–376. [CrossRef]
37. Xu, H.; Wang, C.; Song, Y.; Zhu, J.; Xu, Y.; Yan, J.; Song, Y.; Li, H. CNT/Ag_3PO_4 composites with highly enhanced visible light photocatalytic activity and stability. *Chem. Eng. J.* **2014**, *241*, 35–42. [CrossRef]
38. Jia, T.K.; Zhao, J.W.; Fu, F.; Deng, Z.; Wang, W.M.; Fu, Z.Y.; Meng, F.C. Synthesis, characterization and photcatalytic activity Zn-doped SnO_2/Zn_2SnO_4 coupled nanocomposites. *Int. J. Photoenergy* **2014**, *2014*, 197824. [CrossRef]
39. Feng, W.; Fang, J.; Zhou, G.; Zhang, L.; Lu, S.; Wu, S.; Chen, Y.; Ling, Y.; Fang, Z. Rationally designed Bi@BiOCl/g-C_3N_4 heterostructure with exceptional solar-driven photocatalytic activity. *Mol. Catal.* **2017**, *434*, 69–79. [CrossRef]
40. Shan, W.J.; Hu, Y.; Bai, Z.G.; Zheng, M.M.; Wei, C.H. In situ preparation of g-C_3N_4/bismuth-based oxide nanocomposites with enhanced photocatalytic activity. *Appl. Catal. B* **2016**, *188*, 1–12. [CrossRef]
41. Aghdam, S.M.; Haghighi, M.; Allahyari, S.; Yosefi, L. Precipitation dispersion of various ratios of BiOI/BiOCl nanocomposite over g-C_3N_4 for promoted visible light nanophotocatalyst used in removal of acid orange 7 from water. *J. Photochem. Photobiol. A Chem.* **2017**, *338*, 201–212. [CrossRef]
42. Li, Y.F.; Fang, L.; Jin, R.X.; Yang, Y.; Fang, X.; Xing, Y.; Song, S.Y. Preparation and enhanced visible light photocatalytic activity of novel g-C_3N_4 nanosheetsloaded with Ag_2CO_3 nanoparticles. *Nanoscale* **2015**, *7*, 758–764. [CrossRef] [PubMed]
43. Xu, H.; Yan, J.; Xu, Y.G.; Song, Y.H.; Li, H.M.; Xia, J.X.; Huang, C.J.; Wan, H.L. Novel visible-light-driven AgX/graphite-like C_3N_4 (X = Br, I) hybrid materials with synergistic photocatalytic activity. *Appl. Catal. B* **2013**, *129*, 182–193. [CrossRef]
44. Zhao, H.; Dong, Y.M.; Jiang, P.P.; Miao, H.Y.; Wang, G.L.; Zhang, J.J. In situ light-assisted preparation of MoS_2 on graphitic C_3N_4 nanosheets for enhanced photocatalytic H_2 production from water. *J. Mater. Chem. A* **2015**, *3*, 7375–7381. [CrossRef]
45. Bai, X.J.; Sun, C.P.; Wu, S.L.; Zhu, Y.F. Enhancement of photocatalytic performance via a P3HT-g-C_3N_4 heterojunction. *J. Mater. Chem. A* **2015**, *3*, 2741–2747. [CrossRef]
46. Guo, Y.; Li, J.H.; Gao, Z.Q.; Zhu, X.; Liu, Y.; Wei, Z.B.; Zhao, W.; Sun, C. A simple and effective method for fabricating novel p-n heterojuction photocatalyst g-C_3N_4/$Bi_4Ti_3O_{12}$ and its photocatalytic performances. *Appl. Catal. B Environ.* **2016**, *192*, 57–71. [CrossRef]
47. Dang, X.M.; Zhang, X.F.; Chen, Y.T.; Dong, X.L.; Wang, G.W.; Ma, C.; Zhang, X.X.; Ma, H.C.; Xue, M. Preparation of β-Bi_2O_3/g-C_3N_4 nanosheet p–n junction for enhanced photocatalytic ability under visible light illumination. *J. Nanopart. Res.* **2015**, *17*, 93. [CrossRef]
48. Fu, J.; Tian, Y.L.; Chang, B.B.; Xi, F.N.; Dong, X.P. BiOBr–carbon nitride heterojunctions: Synthesis, enhanced activity and photocatalytic mechanism. *J. Mater. Chem.* **2012**, *22*, 21159–21166. [CrossRef]

49. Liu, G.G.; Zhao, G.X.; Zhou, W.; Liu, Y.Y.; Pang, H.; Zhang, H.B.; Hao, D.; Meng, X.G.; Li, P.; Kako, T.; et al. In situ bond modulation of graphitic carbon nitride to construct p–n homojunctions for enhanced photocatalytic hydrogen production. *Adv. Funct. Mater.* **2016**, *26*, 6822–6829. [CrossRef]
50. Hu, R.; Wang, X.; Dai, S.; Shao, D.; Hayat, T.A. Alsaedi, Application of graphitic carbon nitride for the removal of Pb(II) and aniline from aqueous solutions. *Chem. Eng. J.* **2015**, *260*, 469–477. [CrossRef]
51. Zhu, T.T.; Song, Y.H.; Ji, H.J.; Xu, Y.G.; Song, Y.X.; Xia, J.X.; Yin, S.Y.; Li, Y.T.; Xu, H.; Zhang, Q.; et al. Synthesis of g-C_3N_4/Ag_3VO_4 composites with enhanced photocatalytic activity under visible light irradiation. *Chem. Eng. J.* **2015**, *271*, 96–105. [CrossRef]
52. Li, Y.B.; Zhang, H.M.; Liu, P.R.; Wang, D.; Li, Y.; Zhao, H.J. Cross-linked g-C_3N_4/rGO nanocomposites with tunable band structure and enhanced visible light photocatalytic activity. *Small* **2013**, *9*, 3336–3344. [CrossRef] [PubMed]
53. Li, C.J.; Wang, S.P.; Wang, T.; Wei, Y.J.; Zhang, P.; Gong, J.L. Monoclinic porous $BiVO_4$ networks decorated by discrete g-C_3N_4 nano-islands with tunable coverage for highly efficient photocatalysis. *Small* **2014**, *10*, 2783–2790. [CrossRef] [PubMed]
54. Niu, P.; Zhang, L.L.; Liu, G.; Cheng, H.M. Graphene-like carbon nitride nanosheets for improved photocatalytic activities. *Adv. Funct. Mater.* **2012**, *22*, 4763–4770. [CrossRef]
55. Wang, F.; Li, S.F.; Yu, H.G.; Yu, J.G. In situ anion-exchange synthesis and photocatalytic activity of $Ag_8W_4O_{16}$/AgCl–nanoparticle core–shell nanorods. *J. Mol. Catal. A Chem.* **2011**, *334*, 52–59. [CrossRef]
56. Zhu, A.; Zhao, Q.; Li, X.; Shi, Y. $BiFeO_3$/TiO_2 nanotube arrays composite electrode: Construction, characterization, and enhanced photoelectrochemical properties. *ACS Appl. Mater. Interfaces* **2014**, *6*, 671–679. [CrossRef] [PubMed]
57. Li, Y.; Jin, R.; Fang, Y.; Yang, Y.; Yang, M.; Liu, X.; Xing, Y. In situ loading of Ag_2WO_4 on ultrathin nansheets with highly enhanced photocatalytic performance. *J. Hazard. Mater.* **2016**, *313*, 219–228. [CrossRef] [PubMed]
58. Zhao, L.H.; Zhang, L.H.; Lin, H.J.; Nong, Q.Y.; Cui, M.; Wu, Y.; He, Y.M. Fabrication and characterization of hollow $CdMoO_4$ coupled g-C_3N_4 heterojunction with enhanced photocatalytic activity. *J. Harzard. Mater.* **2015**, *299*, 333–342. [CrossRef] [PubMed]
59. Ke, J.; Liu, J.; Sun, H.; Zhang, H.; Duan, X.; Liang, P.; Li, X.; Tade, M.O.; Liu, S.; Wang, S.B. Facile assembly of Bi_2O_3 and p-MoS_2 for enhanced photocatalytic water oxidation and pollutant degradation. *Appl. Catal. B Environ.* **2017**, *200*, 47–55. [CrossRef]
60. Jia, T.K.; Fu, F.; Long, F.; Min, Z.Y.; Zhao, J.W.; Chen, J.; Li, J.L. Synthesis, characterization and enhanced visible-light photocatalytic activity of Zn_2SnO_4-C nanocomposites with truncated octahedron morphology. *Ceram. Int.* **2016**, *142*, 13893–13899. [CrossRef]
61. Jia, T.K.; Wang, X.F.; Long, F.; Li, J.L.; Kang, Z.F.; Fu, F.; Sun, G.; Chen, J. Visible-light photocatalytic activities of 3D hierarchical Bi_2S_3 architectures assembled by nanoplatelets. *Crystals* **2016**, *6*, 140. [CrossRef]